Supplement of Clim. Past, 15, 1133–1151, 2019
https://doi.org/10.5194/cp-15-1133-2019-supplement

Supplement of

Equilibrium simulations of Marine Isotope Stage 3 climate

Chuncheng Guo et al.

Correspondence to: Chuncheng Guo (chuncheng.guo@norceresearch.no)

1 Model spin-up: sea ice

Simulated time evolution of sea ice area, averaged over the northern and southern hemispheres, is shown in Fig. 2. Both experiments show a small drift at the end of the integration. In the NH, the MIS3 experiment shows a larger minimum sea ice area in September, and a smaller maximum sea ice area in March, compared to the PI experiment. The simulated smaller NH March sea ice area at MIS3, is caused by the large region in the peripheral areas of the Arctic Ocean being defined as land in MIS3, when sea level is lowered by 70 m (see Fig. 2 in the main text). In the PI experiment, these areas are defined as ocean, which are ice covered during winter, resulting in a larger area of sea ice cover, even if the climate is warmer than at MIS3. As will be shown later, sea ice in MIS3 has a larger extent in the NH when excluding the above offset due to changes in the land-sea mask. In the SH, MIS3 features larger sea ice area compared to PI in both seasons, even though the above land-sea effect is at play (mostly in the Weddell Sea and the Ross Sea). In austral winter (September), sea ice area continues to increase throughout the multi-millennial model integration. However, the trend is diminished towards the end of the simulation. In austral summer (March), MIS3 sea ice area is comparable to PI and slowly increases until a sudden jump is detected close to model year 1600. After model year 1800 the simulated sea ice shows little drift in both experiments. The rapid increase in sea ice in the MIS3 experiment mainly arises from changes in the Weddell and Ross Sea areas of the model.

2 Simulated MIS3 climate: precipitation

Annual mean global precipitation decreases by 0.18 mm day^{-1} as a consequence of the colder and more arid climate during MIS3. Geographically, during DJF, a significant decrease in precipitation is seen in the North Pacific, the western North Atlantic, the Barents Sea and in the Nordic Seas (Fig. 3). Greater precipitation is seen in the eastern and subtropical Pacific and in the eastern North Atlantic. Precipitation in the western Labrador Sea also increases, due to the reduced sea ice cover (see Fig. 9 in the main text). In the tropics, precipitation in the African and South American monsoon regions, as well as in the western Pacific warm pool, is remarkably reduced, and a southward shift of the ITCZ occurs. In contrast, during JJA, western and northern Europe as well as the North Pacific features more precipitation; the Indian monsoon region experiences less precipitation, and in the tropics, the ITCZ moves south in the Pacific and north in the Indian Ocean.

3 Modes of variability

In this section, we briefly evaluate the change of two important climate internal variabilities: the El Niño-Southern Oscillation (ENSO) and the Northern Annular Mode (NAM).

The tropical Pacific cools nearly uniformly during MIS3, with a small change in the zonal SST gradient in the eastern Pacific cold tongue and western Pacific warm pool region (see Fig. 7a in the main text). The amplitude of the SST change in the NINO3.4 region (170°W-120°W, 5°S-5°N) during MIS3 is about 1.2 °C relative to PI, with a weak seasonal cycle (Fig. 8a). As a measure of ENSO, the standard deviation (σ) of the detrended monthly SST anomalies in the NINO3.4 region is smaller during MIS3 (0.45 °C) relative to PI (0.58 °C). The reduction is across all months and is greater in boreal autumn and winter (Fig. 8b), leading to a slightly weakened annual cycle of NINO3.4 SST variability. Similar reductions of ENSO variability were reported in CCSM3 and CCSM4 LGM simulations (Otto-Bliesner et al., 2006; Brady et al., 2013) and a CCSM3 MIS3 interstadial simulation (Merkel et al., 2010), but the results show disagreements among the PMIP2 LGM model simulations (Zheng et al., 2008).

MIS3 shows small and negative skewness across most of the year (Fig. 8c); the annual cycle is smaller during MIS3, with the largest discrepancy in boreal summer compared to PI. For the frequency of ENSO events, the NINO3.4 index exhibits most power over 2-5 years for both MIS3 and PI experiments, with the former showing more power in the lower and the latter in the higher end of the range.

Fig. 9 shows the composite anomalies of DJF SST during El Niño years for the MIS3 and PI experiments. An El Niño year is defined here as a year with the NINO3.4 SST anomalies greater than 1.5σ for three consecutive months, with at least one DJF months. The SST anomalies in the tropical Pacific are weaker during MIS3 and have a smaller westward extent. The maximum SST anomalies, centered around 120°W, are $\sim$1.2 °C at MIS3, compared to $\sim$1.5°C in PI. Stronger negative SST anomalies at MIS3 are seen in the subtropical Pacific in both hemispheres. In the southern Indian Ocean, stronger positive SST anomalies are simulated during MIS3, whereas the anomalies are weaker in the eastern and central Indian Ocean relative to PI.

The NAM (also known as the Arctic Oscillation) is defined here as the first empirical orthogonal function (EOF) of the NH (20-90° N) DJF sea level pressure (SLP) anomalies. The NAM-explained winter SLP variance is reduced during MIS3 (27%) relative to PI (30%), with the centre of action over the Arctic slightly weaker and slightly eastward-shifted (Fig. 10a,b). The shape of the EOF pattern is more asymmetric over the Arctic at MIS3. With the presence of large ice sheets during MIS3, the simulated centre of action is weakened relative to PI in the North Pacific and eastern North Atlantic, resulting in a gradient from the mid-latitude to the pole that is weaker during MIS3.

4 MIS3 sensitivity to CO_2 and ice sheet size

Figs. 12, 13, 14 show simulated anomalies of sea surface salinity (SSS), winter sea ice concentration, and AMOC for the sensitivity experiments with reduced CO_2 levels and Laurentide Ice Sheet.

As associated with the weak reduction of the strength of AMOC (Fig. 8 in the main text), changes in SSS, Arctic sea ice concentration, and AMOC geometry are also small. The experiment in which the AMOC weakens the most (e.g. $\sim$4 Sv) is the one with 140 ppm CO_2 (Fig. 14c). In this experiment, the Arctic sea ice concentration also features the largest anomaly (Fig. 13c), especially on the Pacific side and in the Nordic Seas. However, the major convection sites in the model, e.g., Labrador Sea and part of the Nordic Seas are still ice free, therefore the AMOC is not transitioning into a weak state.

5 Other supplementary figures

Figure 1: The modern day river routing map (upper panel) and the new river routing map generated using the MIS3 topography (lower panel). As also mentioned in the main text, the MIS3 routing is objectively generated from realistic modern conditions: where ice sheets are present under MIS3 but not under modern climate the routing is determined from ice sheet elevation; new streams at the edge of the ice sheets are extended to the ocean consistent with orographic gradients; elsewhere, the modern routing is maintained; modern river mouths are extended to the ocean according to orographic gradients.

Figure 4: Barotropic stream functions of ocean circulation in the North Pacific and North Atlantic region for MIS3 (black) and PI (red) simulations. Contour intervals are 10 Sv, with dashed and solid colors denoting positive and negative values, respectively. The barotropic subtropical and subpolar gyres are broadly similar for the MIS3 and PI experiments; additional streamlines in the North Atlantic subpolar region during MIS3 indicate a stronger subpolar gyre.

Figure 5: Simulated MIS3 (black) and PI (red) northward heat transport for a) global atmosphere, ocean, and total, and for b) global ocean, Atlantic Ocean, and Pacific and Indian Ocean. The ocean heat transport is calculated directly from the ocean model, and the atmospheric heat transport is calculated by meridional integration of the difference between the zonal integration of the net TOA and surface heat flux.

Figure 6: Simulated a) MIS3 March, b) MIS3 September, c) PI March, and d) PI September mixed layer depth.

Figure 7: Southern Ocean zonal mean ideal age for NorESM MIS3 (upper panel) and PI (lower panel) experiments, respectively.

Figure 11: Simulated near surface temperature anomaly of MIS3 "stadial" experiment relative to MIS3 interstadial control run (model output averaged between years 2401-2500). The black and magenta lines indicate the 15% March sea ice concentration for the MIS3 interstadial and "stadial" experiments, respectively.

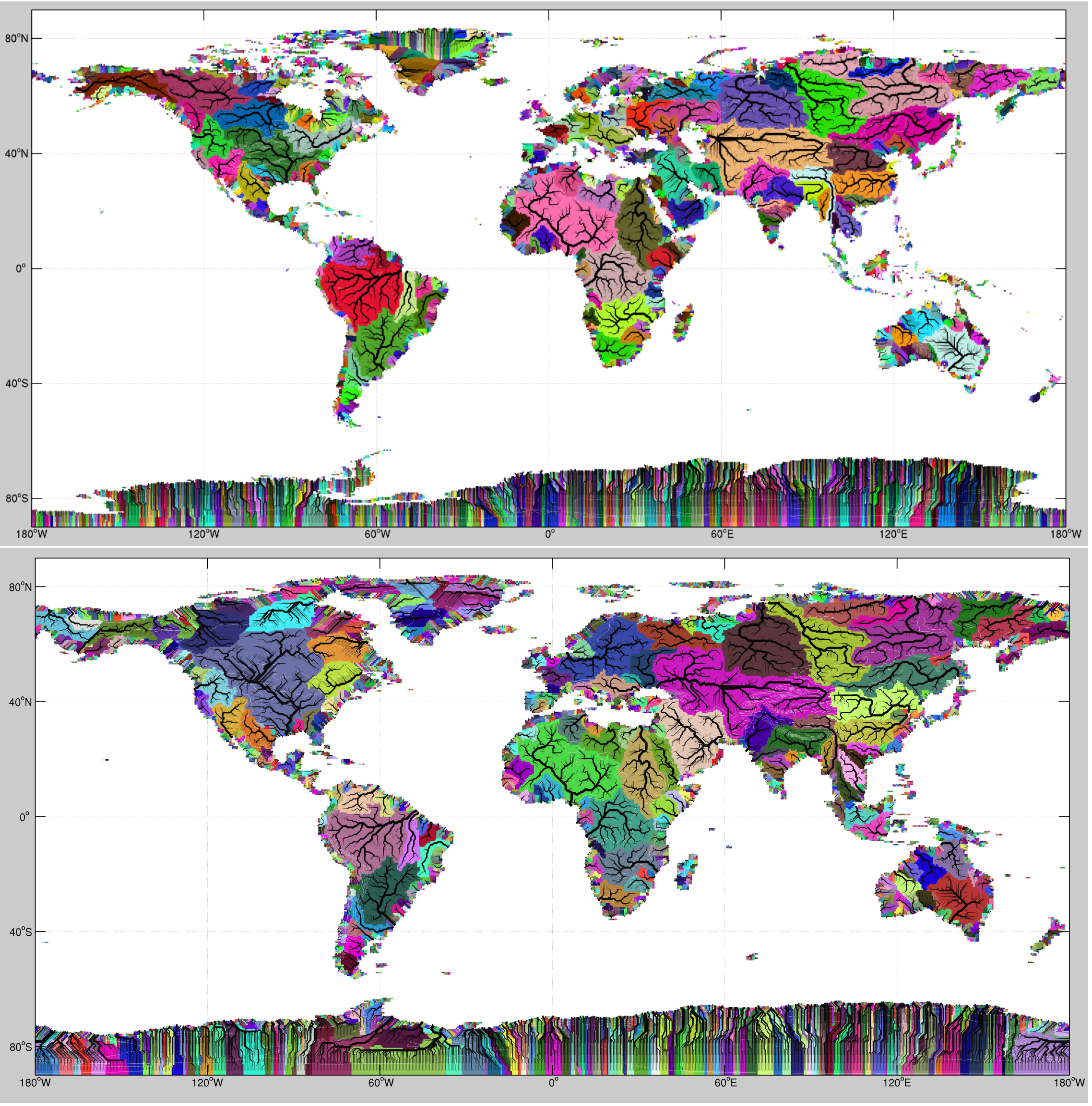

Figure 1. The modern day river routing map (upper panel) and the new river routing map generated using the MIS3 topography (lower panel). As also mentioned in the main text, the MIS3 routing is objectively generated from realistic modern conditions: where ice sheets are present under MIS3 but not under modern climate the routing is determined from ice sheet elevation; new streams at the edge of the ice sheets are extended to the ocean consistent with orographic gradients; elsewhere, the modern routing is maintained; modern river mouths are extended to the ocean according to orographic gradients.

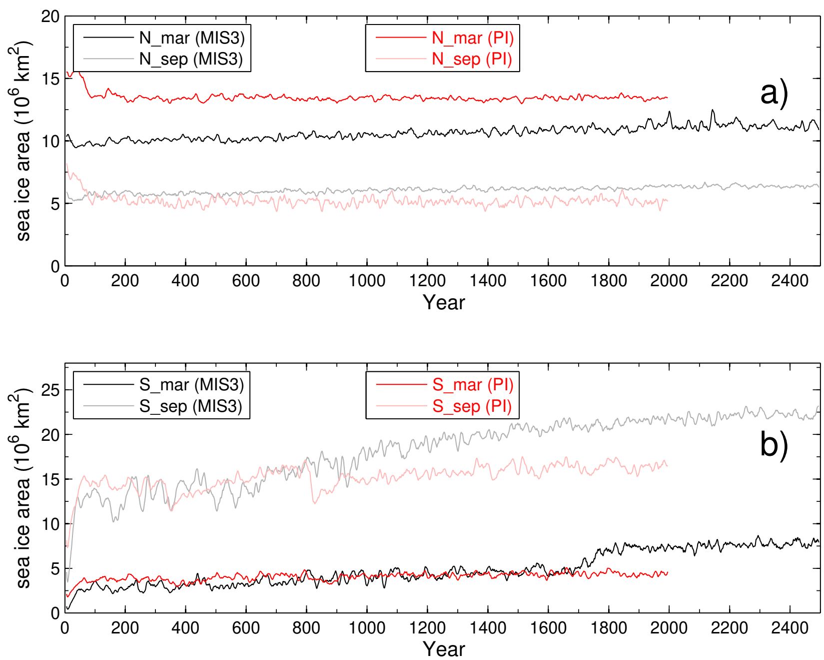

Figure 2. Time series of a) Northern Hemisphere and b) Southern Hemisphere sea ice area for the MIS3 (black) and PI (red) experiments. The data shown are 10-year running mean values.

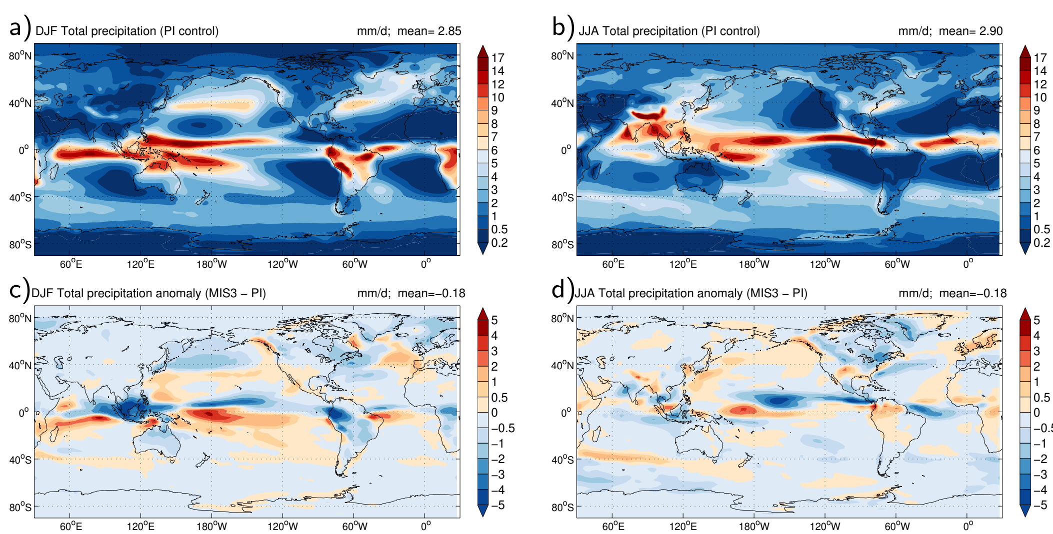

Figure 3. Simulated seasonal (DJF/JJA) total precipitation for a,b) PI and c,d) MIS3 minus PI (mm day^{-1}).

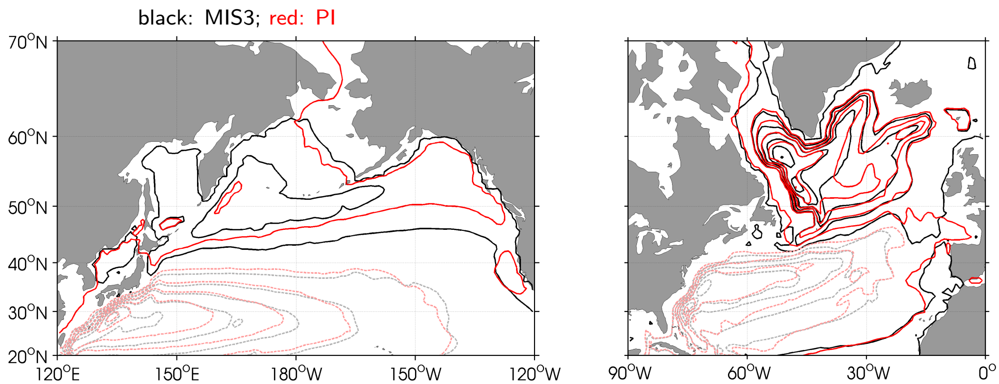

Figure 4. Barotropic stream functions of ocean circulation in the North Pacific and North Atlantic region for MIS3 (black) and PI (red) simulations. Contour intervals are 10 Sv, with dashed and solid colors denoting positive and negative values, respectively. The barotropic subtropical and subpolar gyres are broadly similar for the MIS3 and PI experiments; additional streamlines in the North Atlantic subpolar region during MIS3 indicate a stronger subpolar gyre

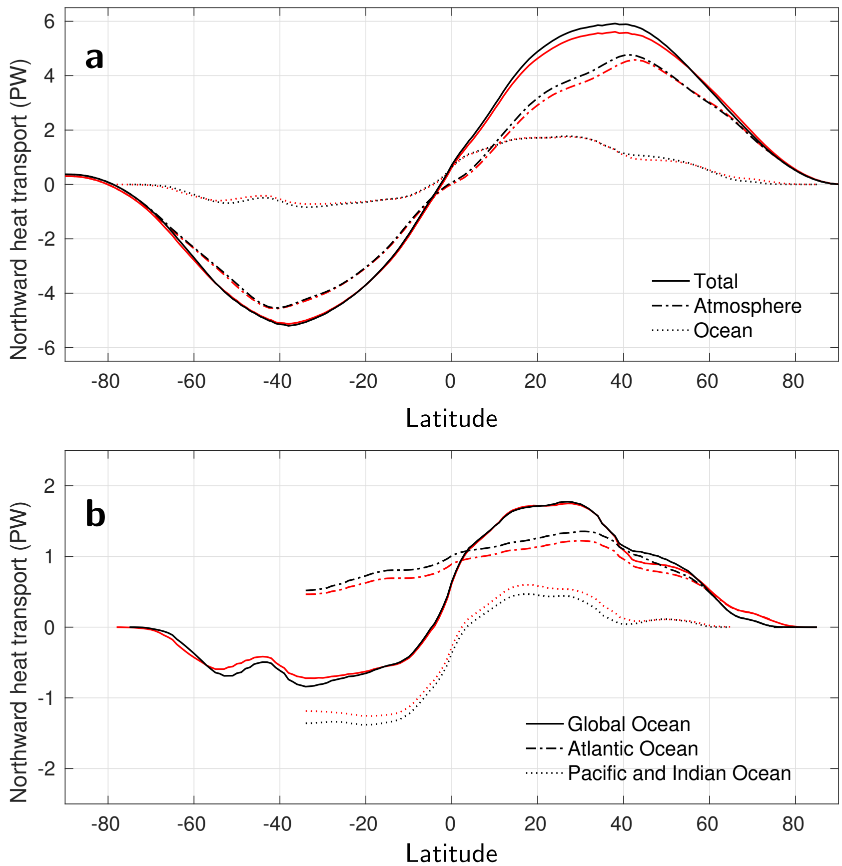

Figure 5. Simulated MIS3 (black) and PI (red) northward heat transport for a) global atmosphere, ocean, and total, and for b) global ocean, Atlantic Ocean, and Pacific and Indian Ocean. The ocean heat transport is calculated directly from the ocean model, and the atmospheric heat transport is calculated by meridional integration of the difference between the zonal integration of the net TOA and surface heat flux.

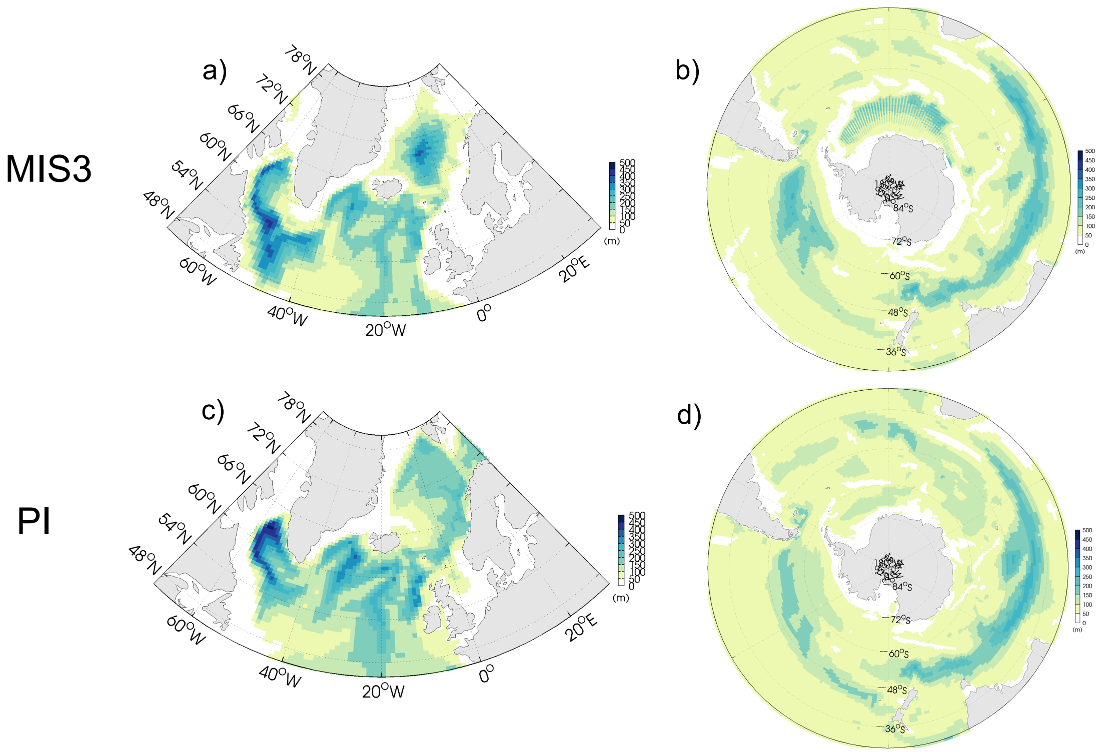

Figure 6. Simulated a) MIS3 March, b) MIS3 September, c) PI March, and d) PI September mixed layer depth.

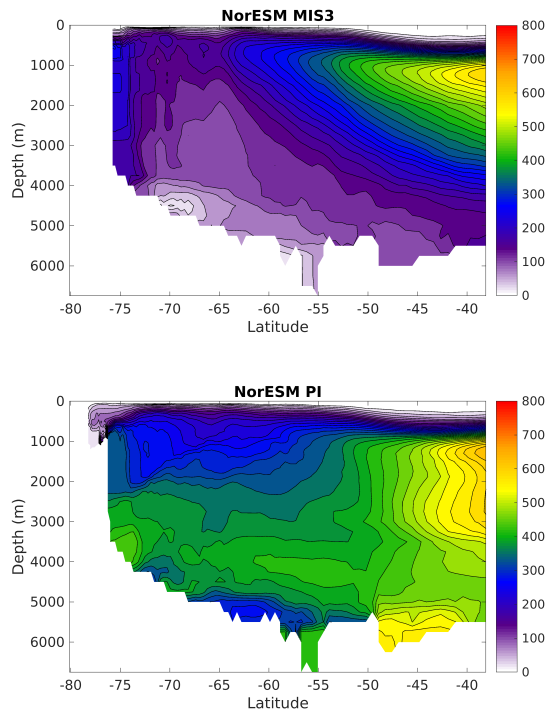

Figure 7. Southern Ocean zonal mean ideal age for NorESM MIS3 (upper panel) and PI (lower panel) experiments, respectively.

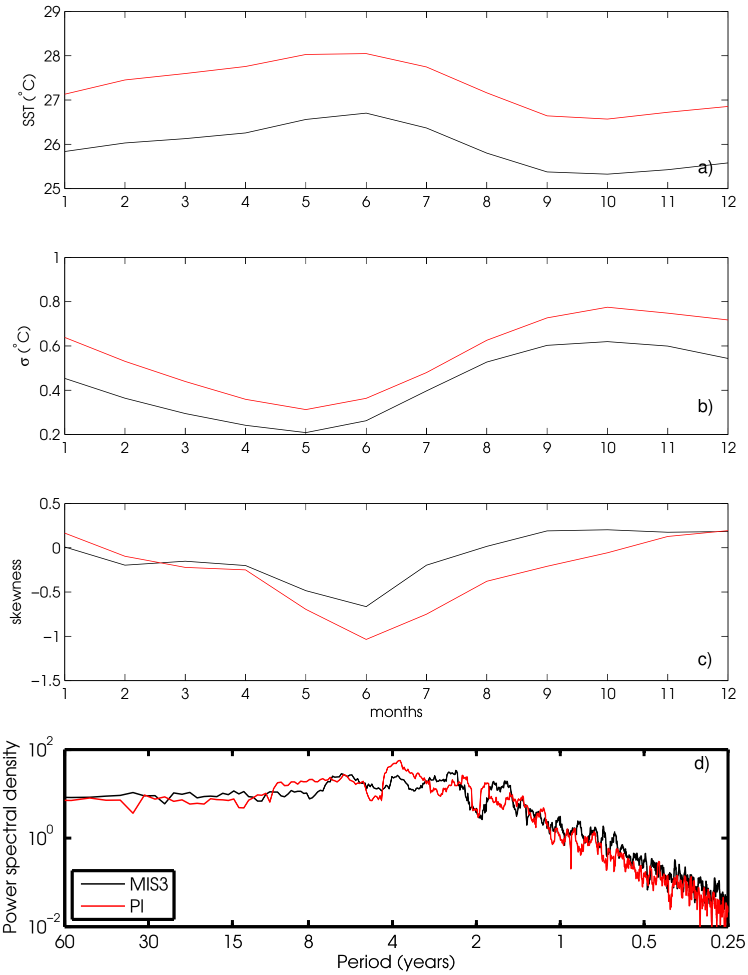

Figure 8. Monthly interannual a) SST, b) standard deviation of SST anomalies, c) skewness of SST anomalies in the NINO3.4 region, and d) power spectra of the NINO3.4 index for the MIS3 and PI, respectively.

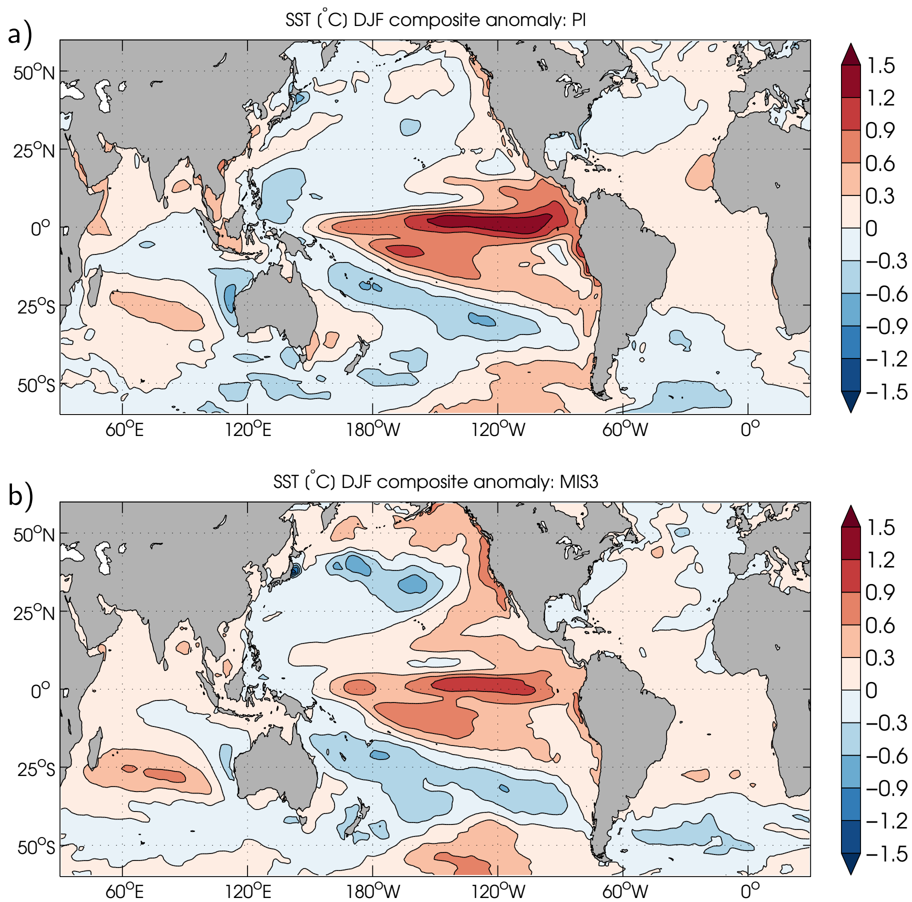

Figure 9. Composite DJF SST anomalies during El Niño years for a) PI and b) MIS3.

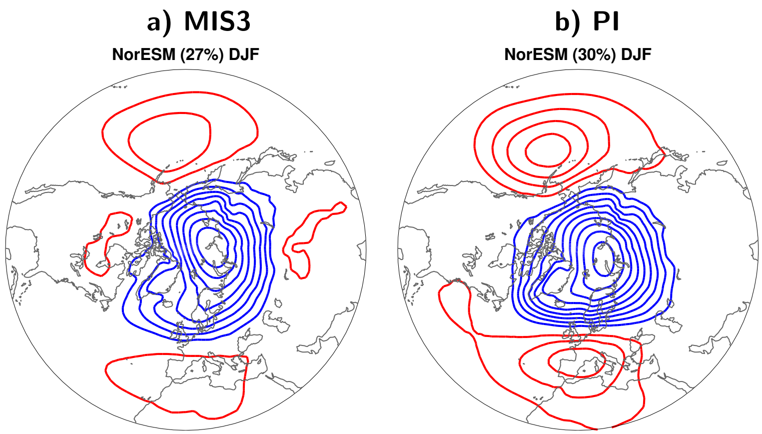

Figure 10. a,b) Leading empirical orthogonal function (EOF) of the winter (DJF) mean sea level pressure (SLP) anomalies over the NH (20-90° N) for a) MIS3 and b) PI. The SLP patterns are obtained by regression of anomalies on the leading principal component time series. The contour intervals in both panels are 1 hPa, with the zero line omitted.

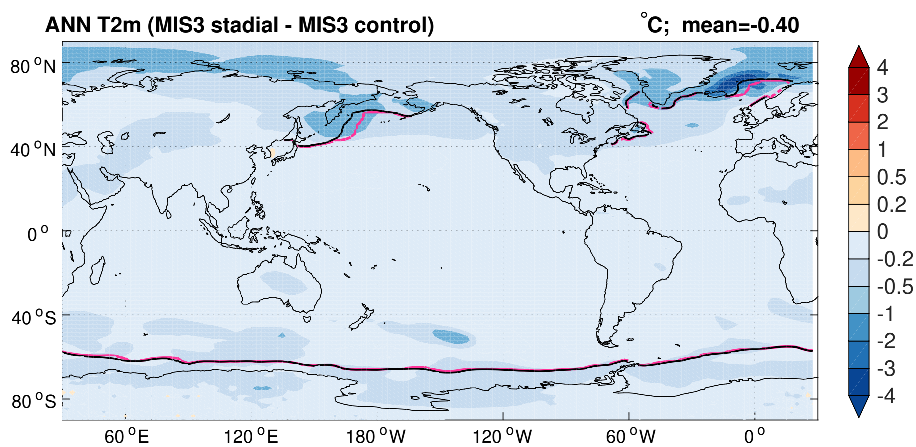

Figure 11. Simulated near surface temperature anomaly of MIS3 "stadial" experiment relative to MIS3 interstadial control run (model output averaged between years 2401-2500). The black and magenta lines indicate the 15% March sea ice concentration for the MIS3 interstadial and "stadial" experiments, respectively.

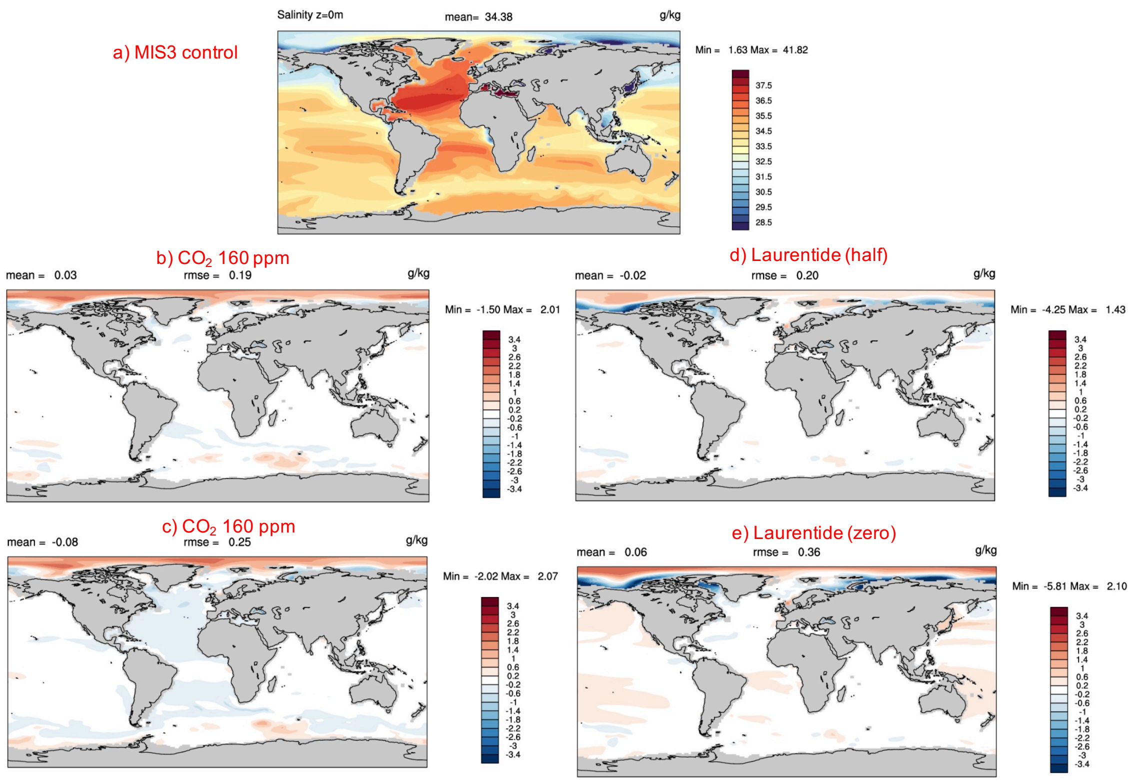

Figure 12. Simulated annual mean sea surface salinity (SSS) for the a) MIS3 control simulation, and the anomalies for the b,c) reduced CO_2 and d,e) reduced Laurentide Ice Sheet sensitivity experiments. The MIS3 control state is the average from years 1901-2000, and the anomalies are averages over the last 100 years of each experiment.

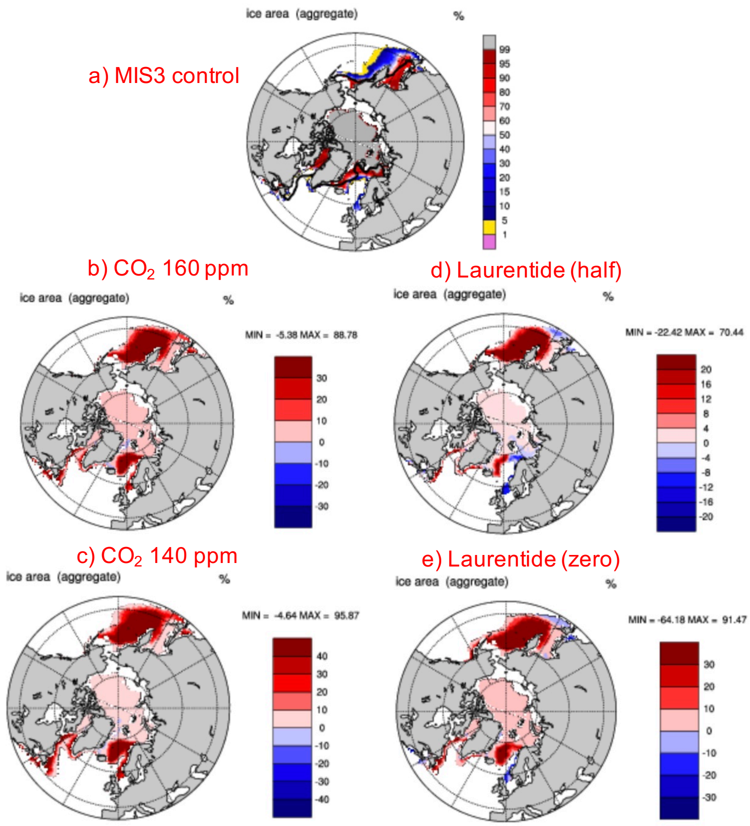

Figure 13. Simulated annual mean winter (January-Feburary-March) Arctic sea ice concentration for the a) MIS3 control simulation, and the anomalies for the b,c) reduced CO_2 and d,e) reduced Laurentide Ice Sheet sensitivity experiments. The MIS3 control state is the average from years 1901-2000, and the anomalies are averages over the last 100 years of each experiment.

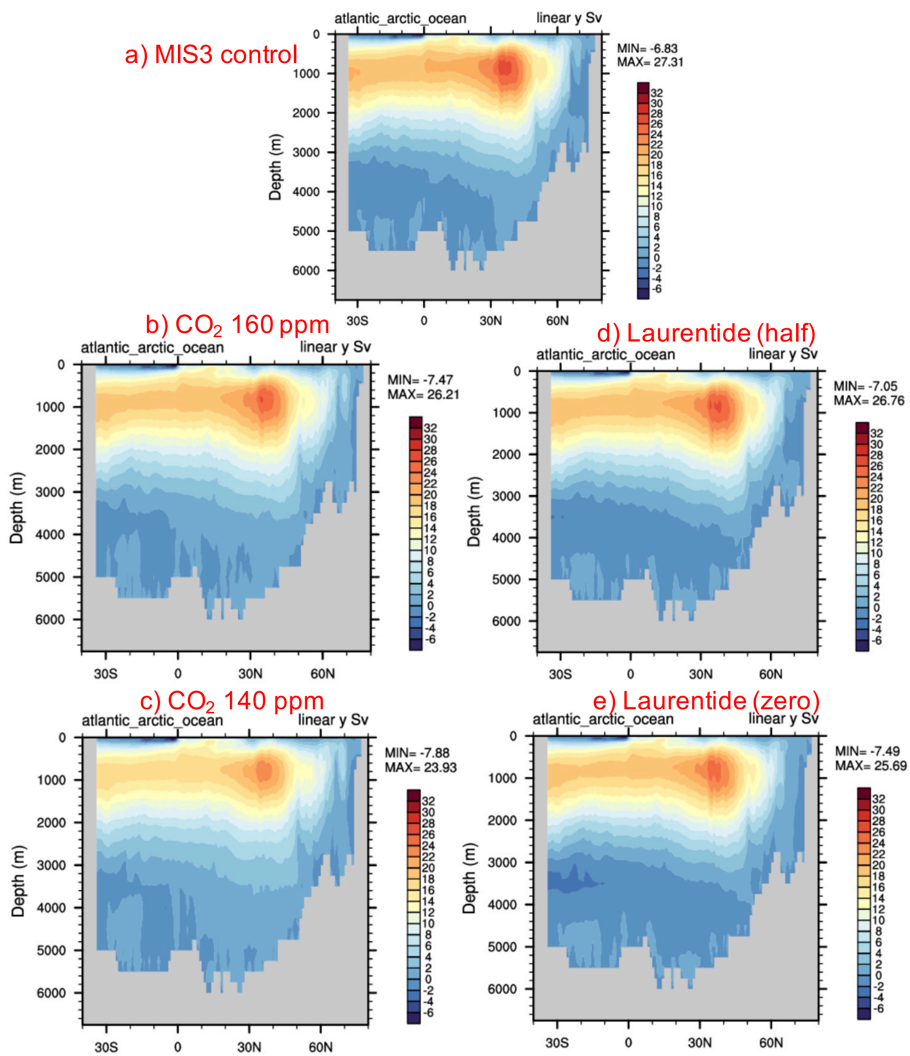

Figure 14. Simulated annual mean AMOC for the a) MIS3 control simulation, b,c) reduced CO_2 and d,e) reduced Laurentide Ice Sheet sensitivity experiments. The MIS3 control state is the average from years 1901-2000, and the anomalies are averages over the last 100 years of each experiment.

References

Brady, E. C., Otto-Bliesner, B. L., Kay, J. E., and Rosenbloom, N.: Sensitivity to Glacial Forcing in the CCSM4, Journal of Climate, 26, 1901–1925, doi:10.1175/JCLI-D-11-00416.1, 2013.

Merkel, U., Prange, M., and Schulz, M.: ENSO variability and teleconnections during glacial climates, Quaternary Science Reviews, 29, 86 – 100, doi:https://doi.org/10.1016/j.quascirev.2009.11.006, climate of the Last Million Years: New Insights from EPICA and Other Records, 2010.

Otto-Bliesner, B. L., Brady, E. C., Clauzet, G., Tomas, R., Levis, S., and Kothavala, Z.: Last Glacial Maximum and Holocene Climate in CCSM3, Journal of Climate, 19, 2526–2544, doi:10.1175/JCLI3748.1, 2006.

Zheng, W., Braconnot, P., Guilyardi, E., Merkel, U., and Yu, Y.: ENSO at 6ka and 21ka from ocean–atmosphere coupled model simulations, Climate Dynamics, 30, 745–762, doi:10.1007/s00382-007-0320-3, 2008.